Source separation techniques applied to the detection of subsurface defects in the eddy current NDT of aeronautical lap-joints

Pierre-Yves Joubert, Eric Vourc'H, Alan Tassin, Yohan Le Diraison

SOURCE SEPARATION TECHNIQUES APPLIED TO THE DETECTION OF SUBSURFACE DEFECTS IN THE EDDY CURRENT NDT OF AERONAUTICAL LAP-JOINTS

P.-Y. JOUBERT, E. VOURC'H, A. TASSIN and Y. LE DIRAISON

SATIE, ENS Cachan, CNRS, UniverSud,

61 Avenue du Président Wilson, 94235 CACHAN Cedex, France

Abstract

This paper investigates the application of two source separation techniques, the principal component analysis and the independent component analysis, to process the data from the eddy current inspection of riveted lap joints. An eddy current array sensor is designed for the rapid inspection of lap-joints and used to test a set of flawed rivet configurations featuring 1 mm to 10 mm long notches, buried down to a 4 mm depth. Implementation methods are proposed for processing such eddy current data by means of both the considered source separation techniques. The signal processing results obtained from the experimental data are compared in terms of source separation efficiency and detection efficiency using a receiver operating characteristic approach. In the light of this study, both the techniques appear to be efficient. However, the principal component analysis better improves the defects detection, especially for deeply buried defects.

Keywords: Eddy current probe, array sensor, riveted lap joint, defect detection, source separation techniques, principal component analysis, independent component analysis, receiver operating characteristic.

Corresponding author: joubert@satie.ens-cachan.fr

1. Introduction

Aircrafts undergo strong thermal and mechanical constraints as well as corrosion that, with time, are likely to weaken and damage their structure. This is particularly true for the riveted lap joints used to maintain together the aluminium parts of the wings and of the fuselage. Indeed, with time, cracks may appear in the vicinity of the rivets [1]. If not detected, they could propagate from one rivet to the other and eventually lead to the wrench of a part of the riveted structure. Therefore, for ageing aircrafts, it is necessary to regularly and thoroughly inspect the riveted lap joints in order to detect cracks in their early stages, to guarantee the safety of operations as well as to optimize the maintenance procedures.

Among the non-destructive testing (NDT) methods used for the in-service inspection of aircraft lap joints, the technique based on eddy currents (EC) is widely used, since it is easy to implement, robust and sensitive to cracks. This method basically consists in inducing EC in the electrically conductive medium, and in measuring the effects of their interactions with the conductivity breaks due to the presence of cracks inside the medium. However, in the case of riveted lap joints, three difficulties arise. Firstly, commercial aircrafts contain hundreds of thousands of rivets and their thorough inspection induces time consuming procedures. Secondly, the cracks are likely to appear in the depth of the riveted structure, and because of the attenuation of the EC intensity within the medium (skin effect) [2] buried cracks are uneasy to detect. Finally, as cracks are likely to appear next to rivet bodies, their interactions with the EC are likely to be masked by the interactions of the rivets themselves with the EC. Indeed, rivets are of much larger dimensions than the cracks and they are present all along the lap-joint structure thickness. For these reasons, conventional procedures carried out by means of “slide probes” are not entirely satisfactory. They are time consuming and prone to human error, because of the interpretation of the measured EC signals is difficult [3].

To overcome these drawbacks, over the last decades the NDE community has developed advanced EC systems to enhance the speed and the accuracy of the inspection, as well as signal processing techniques to provide automatic diagnosis tools. Among the advanced EC systems that have been proposed, one can mention the pulsed eddy current (PEC) sensors, designed to improve the subsurface defect detection by means of a broadband pulse excitation [4]. One can mention high sensitivity magnetometers array probes [5] as well as magneto-optical imagers [6-7] developed to produce a real time detection diagnosis in a large inspection area. One may also mention the eddy current imagers, designed to provide high-resolution EC images of large inspection areas with the implementation of image inversion in view [8]. With regards to the signal processing algorithms that have been implemented, one can mention the principal component analysis (PCA) [9], which was successfully used to extract relevant and robust features either from time-harmonics EC signals [10] or PEC signals [11] relative to defects placed next to lap-joint rivets. Furthermore, it is to be noted that previous works have shown that the PCA could be used as a source separation technique to discriminate the low magnitude EC signatures of buried defects from the dominating high magnitude EC signatures of rivets [8].

In this paper, we report on the application of two source separation techniques to the signals delivered by an EC probe dedicated to the inspection of riveted lap joints. The paper is organized as follows. Section 2 describes the EC probe specifically designed for the rapid detection of defects buried next to rivets in multilayered aeronautical structures. Two operating modes are proposed for this device and they are carried out for the inspection of a riveted lap-joint mock-up featuring subsurface calibrated defects. Section 3 presents the basic principle and proposes implementation procedures for the two source separation techniques that are considered: the PCA and the independent component analysis (ICA). Then, in section 4, a quantitative comparison of these two techniques is done based on the results of the processing of the experimental data. The source separation efficiency of both PCA and ICA is

evaluated by means of a tailor made criterion, and their detection efficiency is characterized using a receiver operating characteristic approach. Finally, section 5 is on conclusions.

2. EC sensor and experimental set up

2.1. Basic principle of the sensor

The proposed EC sensor is made up of a transmitter consisting in a cup-core inducer fed by a time varying driving current I_d, and of a receiver consisting in a set of pickup coils, as depicted in Figure 1. Assuming that the exciting wave generated by the transmitter is plane and that it diffuses in a homogeneous material, the EC density J_z induced at depth z is given by [2]:

$$J_z = J_0 e^{-z\sqrt{\pi f \mu \sigma}} \cos\left(\omega t - z\sqrt{\pi f \mu \sigma}\right) \quad (1)$$

where J_0 is the EC density at the surface of the material, f denotes the frequency of the sinusoidal driving current I_d, and σ and μ are the electrical conductivity and the magnetic permeability of the inspected material respectively. One can note from Equation (1) that the phase-shift $\Delta\varphi$ of the EC density at depth z reads:

$$\Delta\varphi(z) = -z\sqrt{\pi f \mu \sigma} \quad (2)$$

Moreover, the standard skin depth δ, defined as the depth at which the EC density is such that:

$$|J_\delta| = \frac{J_0}{\exp(1)} \quad (3)$$

Hence, δ is given by [2]:

$$\delta = \frac{1}{\sqrt{\sigma \mu \pi f}} \quad (4)$$

which means that 63% of the induced EC are concentrated between $z = 0$ and $z = \delta$.

Here, the structure of the transmitter (Figure 1) is chosen so that when placed exactly above a rivet (i.e. when the revolution axis of the transmitter merges with the revolution axis of the rivet) the induced EC flow circularly around the rivet, that is, following the θ coordinate of the cylindrical coordinate system associated with a rivet. In this way, the interactions between the EC and the rivet are limited. Indeed, the conductivity break due to the air gap existing between the rivet and the aluminium plates hardly modifies the EC flow since they are both collinear to the θ coordinate. On the other hand, in the presence of a defect such as a crack growing from the rivet body along the *r* axis (Figure 1), the EC reach the crack perpendicularly to its orientation, in such a way that the interactions are maximum and give rise to a local magnetic field relative to the defect and featuring a normal component H_z of significant amplitude. In order to sense these interactions, a set of flat pick-up coils sensitive to H_z, is placed under the transmitter. The set of pick-up coils consists in a circular array of 4 coils, denoted A, B, C, and D (Figure 1). Each of them comprises 32 turns distributed on an 8 layers printed circuit board (PCB) and covers an angular sector of 90 degrees (Figure 1 and Figure 3). The four pick-up coils of the array can be connected either for absolute or differential measurements. In the case of absolute measurements, the electromotive forces (EMF) induced at the ends of A, B, C and D, respectively denoted E_A, E_B, E_C and E_D, are measured independently from one another; hence the EC data provided by the sensor are the trans-impedances $Z_A=E_A / I_d$, $Z_B=E_B / I_d$, $Z_C=E_C / I_d$, and $Z_D=E_D / I_d$. With regards to the differential measurements, the EC data are the following differential trans-impedances: $Z_{AB}= (EMF_A - EMF_B) / I_d$ and $Z_{DC} = (EMF_D – EMF_C) / I_d$.

2.2. Operating modes

In this study, two operating modes are considered for the implementation of the sensor. The first one consists in moving the sensor along the rivet line (along the x axis, Figure 2.a.) starting from a

position at which the sensor is exactly centred onto a rivet, and acquiring the EC data at each position of the sensor. Let this continuous scanning acquisition mode be called the S-mode. The second mode consists in acquiring EC data only when the sensor is centred exactly on each rivet, at the P_i positions (Figure 2.b); this "punctual" acquisition mode is called the P-mode. Thanks to the configuration of the sensor the P-mode is theoretically sufficient to detect the presence of defects growing from the rivet, whatever their orientation. Moreover, it allows rapid inspection procedures to be implemented.

2.3. Experimental set-up and EC data

The sensor was used to inspect a laboratory made lap-joint mock-up constituted of five aluminium plates maintained together by removable aluminium rivets (Figure 1). The plates are 2 mm thick, non-magnetic and feature an electrical conductivity of σ = 35 MS / m. The plates also are exchangeable so that calibrated defects can be placed next to the rivets, in plate n°2 or n°3 (Figure 1). The considered defects are 500 µm wide and 2 mm high notches, and they range from 1 mm to 10 mm in length (Table 1). In this study, only defects oriented along the rivet line (x axis on Figure 2) are considered. As a consequence, only the EC data Z_{AB} provided by pick-up coils A and B (Figure 1) are considered. Coils A and B are connected in series and in phase opposition in order to reject the influence of the rivet itself. The sensor is implemented either in S-mode or P-mode by a PC-controlled ISEL 3 axes robot, which exhibits a 10 µm positioning accuracy in each direction. The data are acquired using a PC-controlled HP4192A impedance analyzer. As an example, the EC data obtained at frequency f_2 = 1200 Hz for the inspection of a mock-up configuration comprising 9 sound rivets and one flawed rivet, are presented in Figure 4 (in-phase and quadrature plots) and in Figure 5 (Lissajous plot). In this example, the flawed rivet is positioned at P_7 and features a 5 mm notch positioned in the 2nd plate that grows from the rivet body. In S-mode the acquisition step is 1 mm; in P-mode, the distance between two

successive positions is P_{i+1}-P_i = 40 mm ($i \in$ [1,..., 9]). One can note that in S-mode the presence of the buried defect hardly alters the shape of the EC signature of the rivet, whereas in P-mode it is clearly visible at position P_7, which validates the concept of the sensor. However, in order to improve the detection of buried defects, the authors propose to implement and compare two source separation techniques so as to display more prominently the presence of the defects.

3. EC data processing using source separation techniques

Assuming that the EC data **M** provided by the inspection of a flawed rivet is a linear mixing of physical sources **S**, one can write:

$$\mathbf{M} = \mathbf{T}.\mathbf{S} \Leftrightarrow \begin{Bmatrix} \mathbf{m_1} \\ \mathbf{m_2} \end{Bmatrix} = \begin{bmatrix} t_{11} & t_{12} \\ t_{21} & t_{22} \end{bmatrix} \begin{Bmatrix} \mathbf{s_1} \\ \mathbf{s_2} \end{Bmatrix} \tag{5}$$

where **M** is constituted of the in-phase ($\mathbf{m_1}$) and quadrature ($\mathbf{m_2}$) EC data provided by the sensor, **T** is the transfer matrix of the sensor, and **S** is composed of two sources $\mathbf{s_1}$ (assumed to be relative to the rivet) and $\mathbf{s_2}$ (assumed to be relative to the defect). Under these assumptions, estimating the source s2 separately from s1 can carry out the defect detection. Since **T** is unknown, a direct inversion of **M** cannot be envisaged. However, the independent component analysis (ICA) or the principal component analysis (PCA) used as a source separation technique, are good candidates to estimate $\mathbf{s_2}$ from **M**, under different assumptions. Both these techniques are implemented and compared in the following sections.

3.1. PCA Basic Principle

In the PCA method, the sources are assumed to be centred and uncorrelated [9], so that:

$$\mathbf{SS^T} = \begin{bmatrix} \sigma_1^2 & 0 \\ 0 & \sigma_2^2 \end{bmatrix}, \tag{6}$$

where (^{T}) denotes the conjugate transpose operator and σ_1 and σ_2 are the energy of the sources $\mathbf{s}_1$ and $\mathbf{s}_2$ respectively. Furthermore, the column vectors of **T** are assumed to be orthogonal, which means that **T** can be decomposed as the product of a rotation matrix **R** and a dilatation matrix **D**:

$$\mathbf{T} = \mathbf{R}\,\mathbf{D} = \begin{bmatrix} \cos\theta & -\sin\theta \\ \sin\theta & \cos\theta \end{bmatrix} \begin{bmatrix} d_1 & 0 \\ 0 & d_2 \end{bmatrix} \tag{7}$$

Under these assumptions, the variance-covariance matrix $\mathbf{MM^T}$ reads:

$$\mathbf{MM^T} = \mathbf{TSS^T T^T} = \mathbf{R} \begin{bmatrix} d_1^2\sigma_1^2 & 0 \\ 0 & d_2^2\sigma_2^2 \end{bmatrix} \mathbf{R^T} \tag{8}$$

Besides, the singular value decomposition of $\mathbf{MM^T}$ leads to:

$$\mathbf{MM^T} = \mathbf{V} \begin{bmatrix} \lambda_1 & 0 \\ 0 & \lambda_2 \end{bmatrix} \mathbf{V^T} \tag{9}$$

where $\boldsymbol{V}$ is the matrix of the eigenvectors of $\boldsymbol{M}$ associated to the eigenvalues λ_1 and λ_2, arranged by decreasing order. One can note that Equations (8) and (9) lead to the formal identification of $\boldsymbol{R}$ and $\boldsymbol{V}$. As a consequence, the PCA consists in the computation of $\boldsymbol{V^T M}$ that leads to the estimation $\hat{\mathbf{S}}$ of the sources **S**, since:

$$\mathbf{V^T M} = \mathbf{V^T (T S)} = \mathbf{(V^T R)(D S)} = \begin{bmatrix} d_1 \mathbf{s_1} \\ d_2 \mathbf{s_2} \end{bmatrix} = \hat{\mathbf{S}} \tag{10}$$

Since the vectors of ***R*** and ***T*** appear in an unknown order, the sources are rather separated than estimated. Besides, the vectors of ***V*** are arranged by decreasing order of their eigenvalues. Therefore, in this study, the implementation of the PCA will carry out a source separation in which the first row $\hat{\mathbf{s}}_1$ of $\hat{\mathbf{S}}$ is expected to be relative to the rivet (as the rivets feature the highest contribution to the EC signals) and the second row $\hat{\mathbf{s}}_2$ is expected to be relative to the defect (as the defects feature a lower contribution to the EC signals).

3.2. PCA Implementation

The efficiency of the source separation techniques is related to the satisfaction of the assumptions expressed in Equations 3 and 5, which are not entirely satisfied in the case of EC data [8]. However, the PCA is known to carry out a good rejection of the source of highest contribution (rivet) while estimating the sources of lower contribution (defects), even if the assumptions are not fully satisfied [9]. This feature is well fitted to the considered case of defect detection.

Furthermore, the excitation frequency can be optimized so that the assumptions are approached, if not entirely fulfilled [8]. Indeed, previous works have shown that the separation efficiency is enhanced when the frequency of the EC is chosen so that the phase-shift (Equation (2)) of the EC flowing at the depth of the flaw, denoted z_{flaw}, is such that:

$$\Delta\varphi(z_{flaw}) = -\frac{\pi}{2}. \tag{11}$$

This choice is consistent with the orthogonality assumptions of the column vectors of *T*. According to this frequency optimization, we chose the frequencies f_2 = 1200 Hz and f_3 = 500 Hz for the detection of the defects positioned in the plates number 2 and 3 respectively.

As an example, the PCA was applied to the raw EC signals of Figure 4, which were obtained at frequency f_2 for the inspection of 9 sound rivets and of one flawed rivet featuring a 5 mm notch positioned in plate 2. According to the PCA results shown in Figure 6, the first PCA component $\hat{s}_1$, which is mainly due to the rivet, is hardly modified by the presence of the defect in P_7. On the other hand, the second PCA component $\hat{s}_2$, which is mainly due to the defect, clearly highlights its presence in P_7, whether over the whole rivet signature (S-mode) or only on the central peak of the signature (P-mode). These results confirm the source separation ability of the PCA.

3.3. ICA principle and implementation

The ICA method is based on an extension of the central limit theorem [12], which states that the distribution of the linear mixing of two independent sources exhibits a higher gaussianity than the distribution of each source. The gaussianity of a signal *s* can be estimated by the kurtosis criterion [12], expressed in Equation (12), which tends to zero for a Gaussian signal:

$$kurt(s) = E[(s-\bar{s})^4] - 3(E[s-\bar{s}^2])^2, \quad (12)$$

where *E(.)* denotes the expectancy. Hence, the estimation of non-Gaussian independent sources consists in finding the linear combination of the considered signals that maximizes the absolute value of the kurtosis [12]. However, the comparison of the kurtosis values is only consistent if calculated for signals that are centred and of unity variance.

Therefore, the implementation of the ICA requires a preliminary whitening step [12,13], which can be performed by means of a PCA of the variance-covariance matrix $\mathbf{MM^T}$ of the measurements. The whitened measurement matrix then reads:

$$\tilde{\mathbf{M}} = \mathbf{V}\begin{bmatrix} \lambda_1 & 0 \\ 0 & \lambda_2 \end{bmatrix}^{-1/2} \mathbf{V^T M} \,. \tag{13}$$

The implementation of the ICA then consists in researching the optimum rotation angle $\theta = \theta_{opt}$, so that:

$$\left| kurt_{\max} \right| = \left| kurt\left(\begin{bmatrix} \cos\theta_{opt} \\ \sin\theta_{opt} \end{bmatrix} \tilde{\mathbf{M}} \right) \right| . \tag{14}$$

Finally, the sources estimated by ICA read:

$$\hat{\mathbf{S}} = \begin{bmatrix} \cos\theta_{opt} & -\sin\theta_{opt} \\ \sin\theta_{opt} & \cos\theta_{opt} \end{bmatrix} \tilde{\mathbf{M}} \,. \tag{15}$$

Conversely to the PCA (section 3.2.), the sources estimated using ICA are not likely to appear in a predefined order. Hence, the identification of the sources requires a calibration step, which is carried out on known flawed situations. In this study, in order to make the comparison with the PCA results easier, the source relative to the rivet is placed in $\hat{\mathbf{s}}_1$ and the source relative to the defect is placed on $\hat{\mathbf{s}}_2$.

As an illustration, the ICA is implemented for the processing of the raw EC data presented in Figure 4. The estimated sources of $\hat{\mathbf{S}}$ are determined using Equation (15), and presented in Figure 7. One can note that like the PCA, the ICA operates a source separation in which $\hat{\mathbf{s}}_1$ is mostly due to the rivets, whereas $\hat{\mathbf{s}}_2$ clearly highlights the presence of the defect in P_7 either in S-mode or in P-mode.

4. Evaluation of PCA and ICA efficiency for defect detection

In order to quantitatively compare the efficiency of the two considered source separation techniques, we firstly evaluate the source separation efficiency, and secondly the defect detection efficiency, of both PCA and ICA methods.

4.1. Source separation efficiency

In this section, the source separation efficiency is studied for various flawed rivet configurations, and quantified by means of a separation criterion, as developed in the following subsection.

4.1.1 Source separation ratio

In order to quantitatively evaluate the efficiency of the separation, we build the normalized source separation ratios (NSSR) $\hat{S}_{1N}$ and $\hat{S}_{2N}$, expressed in dB:

$$\hat{S}_{1N} = 10\log_{10}\left(\frac{\hat{S}_1}{\hat{S}_{1ref}}\right)$$
$$\hat{S}_{2N} = 10\log_{10}\left(\frac{\hat{S}_2}{\hat{S}_{2ref}}\right) \quad (16)$$

where $\hat{S}_1$ and $\hat{S}_2$ are the energies of the sources $\hat{\mathbf{s}}_1$ (rivet) and $\hat{\mathbf{s}}_2$ (defect) respectively, both computed on a window of width $W+1$ along the x-axis, centred onto the rivet position P_i:

$$\hat{S}_1 = \sum_{x=P_i-\frac{W}{2}}^{P_i+\frac{W}{2}} \hat{\mathbf{s}}_1^2(x)$$
$$\hat{S}_2 = \sum_{x=P_i-\frac{W}{2}}^{P_i+\frac{W}{2}} \hat{\mathbf{s}}_2^2(x) \quad (17)$$

and where $\hat{S}_{1ref}$ and $\hat{S}_{2ref}$ are the reference energy values of $\hat{\mathbf{s}}_1$ and $\hat{\mathbf{s}}_2$ respectively, determined from ten sound rivet configurations:

$$\hat{S}_{1ref} = \frac{1}{10}\sum_{i=1}^{10}\sum_{x=P_i-\frac{W}{2}}^{P_i+\frac{W}{2}}\hat{\mathbf{s}}_1^2(x)$$
$$\hat{S}_{2ref} = \frac{1}{10}\sum_{i=1}^{10}\sum_{x=P_i-\frac{W}{2}}^{P_i+\frac{W}{2}}\hat{\mathbf{s}}_2^2(x) \quad (18)$$

Note that for either the flawed or reference configuration, the width of the window on which the NSSR is calculated is defined by $W = 20$ in the case of S-mode EC data, and $W = 0$ in the case of P-mode EC data.

4.1.2. Source separation implementation and results

The PCA and ICA separation methods were applied to EC data resulting from the inspection of a set of 20 flawed rivet configurations, featuring subsurface notches growing from the rivet body in plate n°2 or n°3 (Figure 1), and featuring lengths ranging from 1 mm to 10 mm, as gathered in Table 1. The separation efficiency is evaluated by considering the NSSR determined for both PCA and ICA methods applied to S-mode and P-mode EC data. As a result, Figure 8 and Figure 9 plot $\hat{S}_{2N}$ versus $\hat{S}_{1N}$, for defects buried in the plates number 2 and 3 respectively.

With regards to the separation results shown in Figure 8, the separation efficiency of the PCA is obvious. Indeed, for both the S-mode and the P-mode EC data, $\hat{S}_{2N}$ increases monotonously with the defect length (ranging from 1 mm to 9 mm), while $\hat{S}_{1N}$ is hardly modified by the presence of the defect. The defect source ($\hat{\mathbf{s}}_2$) is thus clearly separated from the rivet source ($\hat{\mathbf{s}}_1$), and vice versa. In the case of the ICA, one can note that $\hat{S}_{2N}$ increases with the defect length for both S-mode and P-mode EC data. However, the length of the defect also alters $\hat{S}_{1N}$: the source separation is less efficient than with the PCA.

The same conclusion can be derived from the separation results obtained by PCA and ICA applied to the EC data relative to defects buried in plate number 3 (Figure 9). Here again, one can note that the PCA operates an efficient source separation, and that the poorest separation results are obtained with the ICA applied to P-mode EC data, too.

Besides, $\hat{S}_{2N}$ appears to decrease when the defects are longer than 9 mm. This behaviour originates from the structure of the used EC probe. Indeed, the distance between the pick-up coils and the revolution axis of the sensor is too short to correctly sense the magnetic field appearing at the end of radial defects longer than 9 mm. In these cases, the sensor sensitivity to the defect is lower, whereas the sensitivity to the rivet remains unchanged. As a consequence, the rejection of the rivet source becomes more difficult than for slightly shorter defects.

As a conclusion, the PCA appears to be more suitable for our source separation problem. Indeed, the assumptions under which the PCA and ICA operate are not entirely satisfied. In particular, the linearity assumption expressed in Equation 5 is not completely satisfied in the case of EC techniques, although often assumed for simplification reasons in the case of small defects [14]. However, even in these conditions, the PCA operates a good rejection of the sources of large energy (rivet) when estimating those of lower energy (defects). This makes the PCA less sensitive than the ICA to an incomplete satisfaction of the assumptions.

4.2. Defect detection efficiency

In order to evaluate the robustness of the defect detection of the PCA and ICA techniques, we consider an enlarged EC data set including the effects of sensor mispositioning. The detection results are evaluated using the receiver operating characteristic (ROC) approach [15], as described in the next subsection.

4.2.1. Basic principle of the receiver operational characteristic

The evaluation of the detection using the ROC approach lies in the statistical test of two assumptions A_0 and A_1:

$$\begin{aligned} &A_0\text{: absence of defect} \\ &A_1\text{: presence of a defect.} \end{aligned} \tag{19}$$

which are relative to the following defect detection procedure:

$$\begin{aligned} &A = A_1 \text{ if } \hat{S}_2 > \lambda \\ &A = A_0 \text{ if } \hat{S}_2 \leq \lambda, \end{aligned} \tag{20}$$

where λ is an adjustable threshold value ranging from $\hat{S}_{2\text{ref}}$ (value of $\hat{S}_2$ obtained after a source separation for the reference sound rivet configuration) to $\hat{S}_{2\text{max}}$ (maximum value of $\hat{S}_2$ resulting from a source separation applied to the considered EC data set). The defect detection procedure is then characterized by the probabilities of good detection (PGD) and of false alarm (PFA) defined by [15]:

$$\begin{aligned} &\text{PGD = probability of deciding } A_1 \text{ knowing } A_1. \\ &\text{PFA = probability of deciding } A_1 \text{ knowing } A_0 \end{aligned} \tag{21}$$

which are used to plot the ROC curve in the (PFA, PGD) plane (or ROC plane), so that:

$$\text{ROC}(\lambda) = (\text{PFA}(\lambda), \text{PGD}(\lambda)) \tag{22}$$

In the (ROC) plane, the point M(1,0), for which PGD = 1 and PFA = 0, is the optimal detection point while M(0,1) is the worst detection point, where the detection is systematically false, and point M(1,1) where any signal value provokes a detection, whatever true or false. ROC curves evolving above the M(0,0) – M(1,1) path in the ROC plane are generally considered to be relative to valid detection algorithms. Besides, the threshold value λ that minimizes the distance from the ROC curve to the optimal detection point M(1,1) is generally considered as providing the best detection adjustment [15]. Moreover, it has been demonstrated that the area under the ROC curve (AUC) is an appropriate criterion to quantitatively compare the efficiency of different detection methods [16]. In the following section, the ROC approach is implemented and the AUC criterion is calculated to quantitatively compare the detection results given by the ICA and PCA source separation methods.

4.2.1. Implementation and results

An enlarged set of EC data relative to flawed and sound rivet configurations was built so as to include experimental discrepancies due to sensor mispositioning. To do so, 10 sound rivet configurations and the 20 flawed rivet configurations of Table 1 are considered. For these 30 configurations, the acquisition of the EC data is repeated with various probe lift-offs $l_0 \in \{0\ \mu m, 50\ \mu m, 100\ \mu m, 150\ \mu m\}$ and various starting points of the probe displacement along the x-axis, $x_0 \in \{0\ \mu m, 250\ \mu m, 500\ \mu m\}$ (Figure 2). As a result, 120 EC data relative to sound rivet configurations, as well as 240 EC data relative to flawed configurations are considered, for each EC acquisition mode. Then, we apply the detection algorithm of Equation (18) to the S-mode and P-mode EC data processed by PCA and ICA, and we compute the PGD and PFA according to Equation (19). The resulting ROC curves are shown in Figure 10 and Figure 11 for the detection of defects placed in the second and third plates, respectively. The AUC, which were

computed for the considered detection cases, are gathered in Table 2. According to Figure 10 and Table 2 (defects in plate n°2) the PCA and ICA detection results are quite close, however, the ACI shows slightly better detection results, possibly due to a better robustness to the experimental noise (sensor mispositioning). On the other hand, considering the detection results of the defects in plate n°3 (Figure 11 and in Table 2), one can note that the PCA based detection obviously shows better performance. Such results can be attributed to the ability of the PCA to reject the source of high energy (rivet) when estimating the lower source (defect), which is particularly relevant for the detection of deeply buried defects in spite of experimental noise. Furthermore, one can note that both the PCA and the ICA based detection algorithms applied to P-mode EC data give lower detection results than when applied to S-mode EC data. Indeed, the P-mode EC data are relative to a unique acquisition point ($W = 0$ in Equation (17)) and therefore they are more sensitive to the sensor positioning than the S-mode data that are constituted of 41 acquisition points ($W = 20$). Nevertheless, as far as the acquisition time is concerned, the P-mode is quite interesting since the EC data are acquired without sensor scanning operations.

5. Conclusion

In this paper the authors consider the EC signals provided by an original EC array sensor designed for the rapid inspection of aeronautical riveted lap joints. The sensor was used either in a conventional scanning mode, or in a punctual mode in which a single sensor position is required to inspect a rivet area. The measured signals were then processed using PCA and ICA based source separation techniques, in order to improve the detection of defects buried within the lap joint and partly masked by the presence of the rivets. The sources separations techniques were implemented for the detection of 1 mm to 10 mm long notches, buried down to a 4 mm depth next to rivets. For these configurations, the two separation techniques were quantitatively compared in terms of source

separation efficiency, and defect detection efficiency using a ROC curve analysis. Both ICA and PCA methods appear to be suited for defect detection, however the PCA has proved to be more efficient to highlight the presence of defects in the case of deeply buried defects. Further works will focus on the extension of the method to the detection of defect of any orientation, as well as on the implementation of multifrequency source separation techniques, so as to consider defect characterization.

6. Acknowledgements

This work was partly supported by grants from Région Ile-de-France in the framework of the competitiveness cluster SYSTEM@TIC PARIS-REGION (Digital Production project).

7. References

1. Ramakrishnan R, Jury D. Characterization of defects and damage in rivet holes in a crown lap joint of a commercial aircraft at design service goal. In: Proceedings of 9th Joint FAA/DoD/NASA Aging Aircraft Conference, Atlanta, USA, 2006.
2. Libby HL, Introduction to electromagnetic nondestructive test methods. New York: Robert Kriegger Publisher Company, 1979.
3. Moore D and Spencer F. Interlayer Crack Detection Results Using Sliding Probe Eddy Current Procedures, in: Proceedings of 10th Asia-Pacific Conference on Non-Destructive Testing, Brisbane, Australia, 2001.
4. Chen T, Tian G Y, Sophian A, Que P. Feature extraction and selection for defect classification of pulsed eddy current NDT, NDT&E International 41 (2008) 467– 476.
5. Dolabdjian C, Wache G, Perez L. Improvement in the detection of subsurface fatigue cracks under airframe fasteners using improved rotating giant magneto-resistance magnetometer head. INSIGHT 2007; 49(3): 133-136.

6. Fitzpatrick GL, Thomes DK, Skaugset RL, Shih EYC, Shih WCL. Magneto-optic / eddy current imaging of aging aircrafts, Material Evaluation. 1993; 51(12): 1402-1407.
7. Development of an improved magneto optic/eddy current imager, final report DOT/FAA/AR-97/37, Office of Aviation Research, Washington DC 1998, 20591.
8. Le Diraison Y, Joubert P-Y, Placko D. Characterization of subsurface defects in aeronautical riveted lap-joints using multi-frequency eddy current imaging. NDT & E International 2009; 42 (2): 133-140.
9. Jolliffe T. Principal Component Analysis, Springer Verlag, New York, 2002
10. Lingvall F, Stepinski T. Automatic Detecting and Classifying Defects During Eddy Current Inspection of Riveted Lap Joints. NDT&E International 2000; 33(1): 47–55.
11. Sophian A, Tian GY, Taylor D, Rudlin J. A Feature Extraction Technique Based On Principal Component Analysis For Pulsed Eddy Current NDT. NDT&E International 36 (2003) 37-41.
12. Hyvärinen A, Karhunen J, Oja E. Independent Component Analysis, John Wiley and sons; 2001.
13. Mardia KV, Kent JT and Bibby JM. Multivariate Analysis, New York: Academic Press, 2000.
14. Sabbagh HA and Sabbagh LD, An eddy current model for 3D-inversion. IEEE Trans on Magnetics, (4): 282-291, 1986
15 Egan JP. Signal detection theory and ROC analysis, Series in cognition and perception, New York, Academic press, 1975.
16 Bradley AP. The use of the area under the ROC curve in the evaluation of machine learning algorithms pattern recognition letters, 30(7): 1145-1159, 1997.

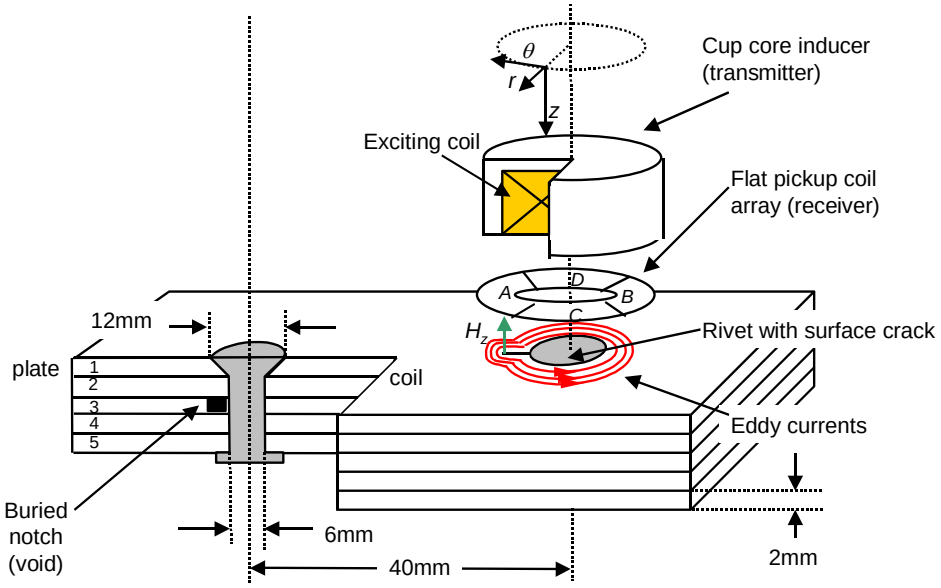

Figure 1. EC sensor configuration and inspected riveted lap joint

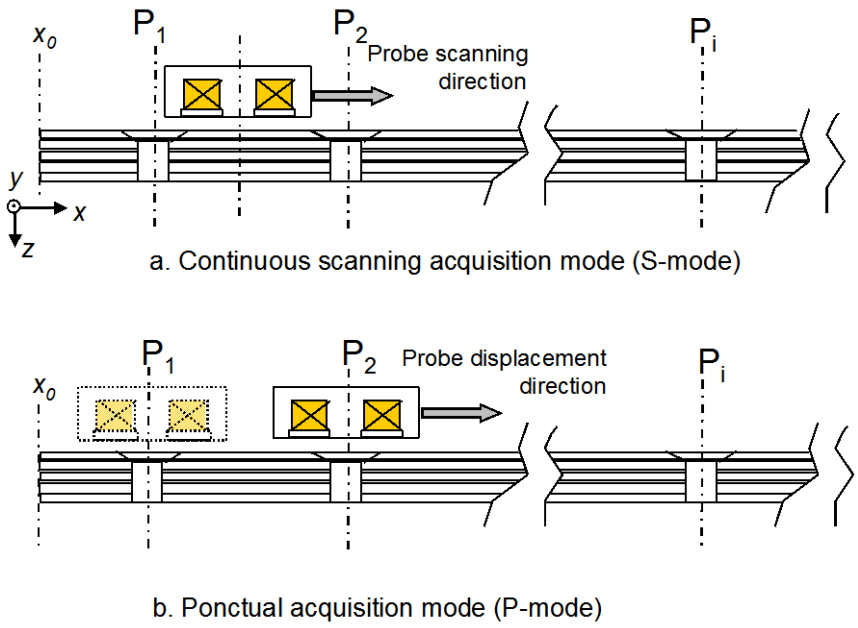

Figure 2. Operating modes

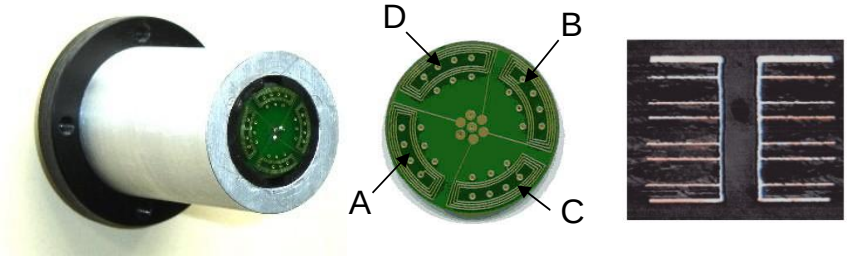

i. Side view of the EC sensor

ii. Flat pick-up coil array (32 turns, 8 layers)

iii. Cut view of the 8-layer PCB structure of a pick-up connexion

Figure 3. Array sensor general view and flat 8-layer circular pick-up coil array

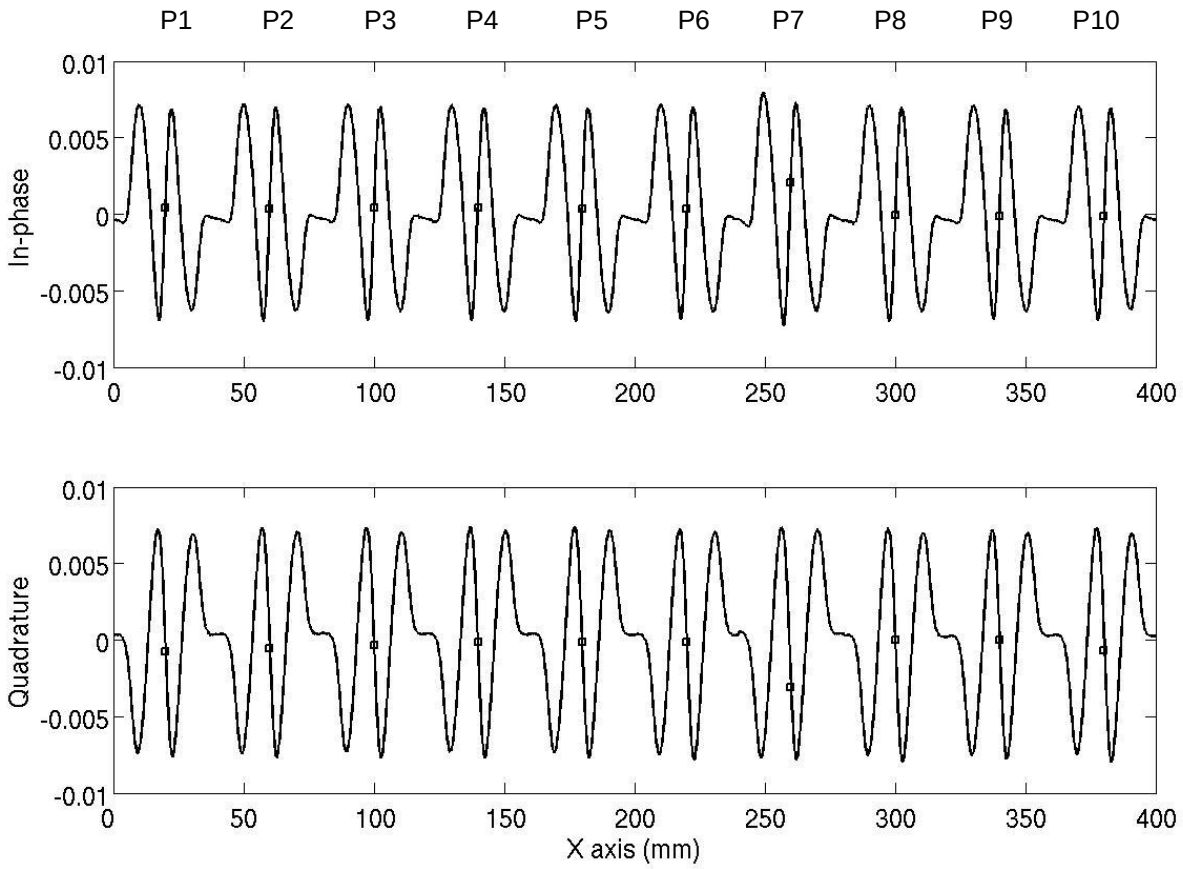

Figure 4. EC signal obtained in S-mode (continuous line) and P-mode (square markers) at 1200Hz for the inspection of 10 rivets (9 rivets are sound, and the rivet in position P7 features a 5mm notch growing from the rivet, in plate 2. Amplitudes of in-phase and quadrature signals are in arbitrary units.

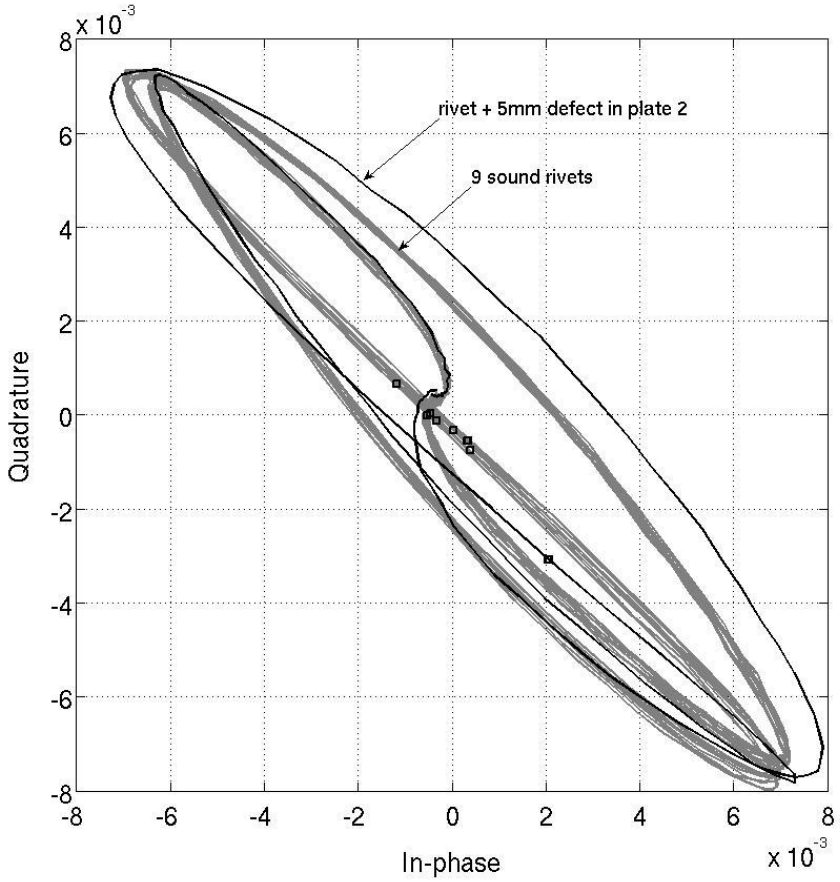

Figure 5. Lissajous plot of the EC signals of Figure 4, S-mode data (black lines: sound rivets; grey lines: flawed rivet) and P-mode data (square markers).

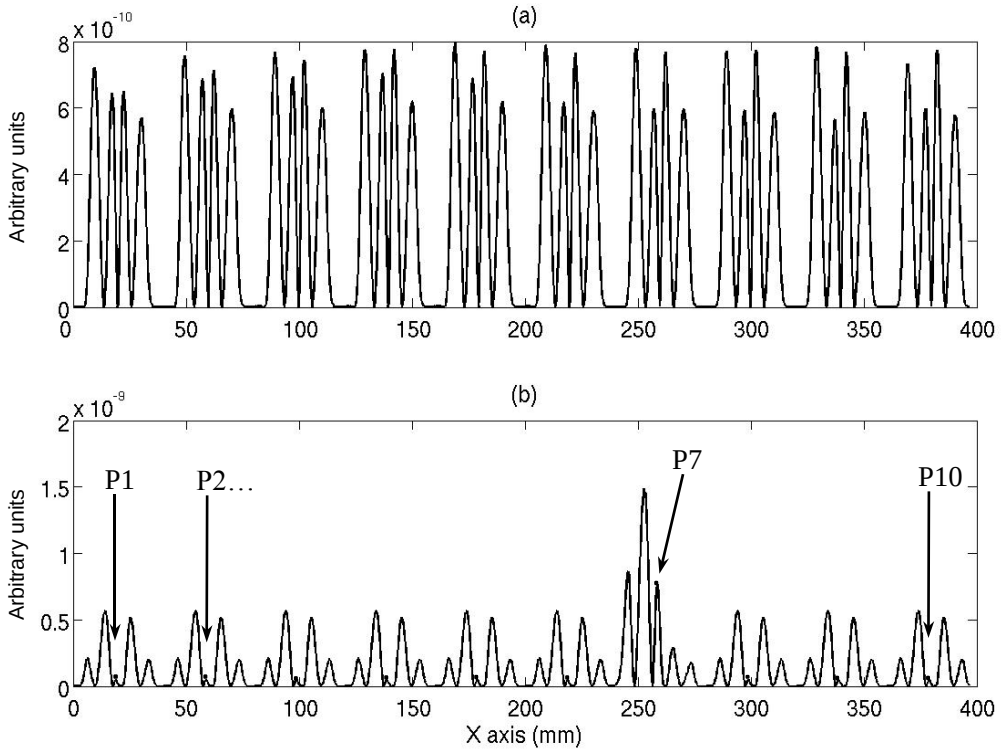

Figure 6. Results of the PCA applied to the EC data of Figure 4. a) Modulus of estimated source $\hat{\mathbf{s}}_1$, b) Modulus of estimated source $\hat{\mathbf{s}}_2$. S-mode data (continuous line), P-mode data (square markers).

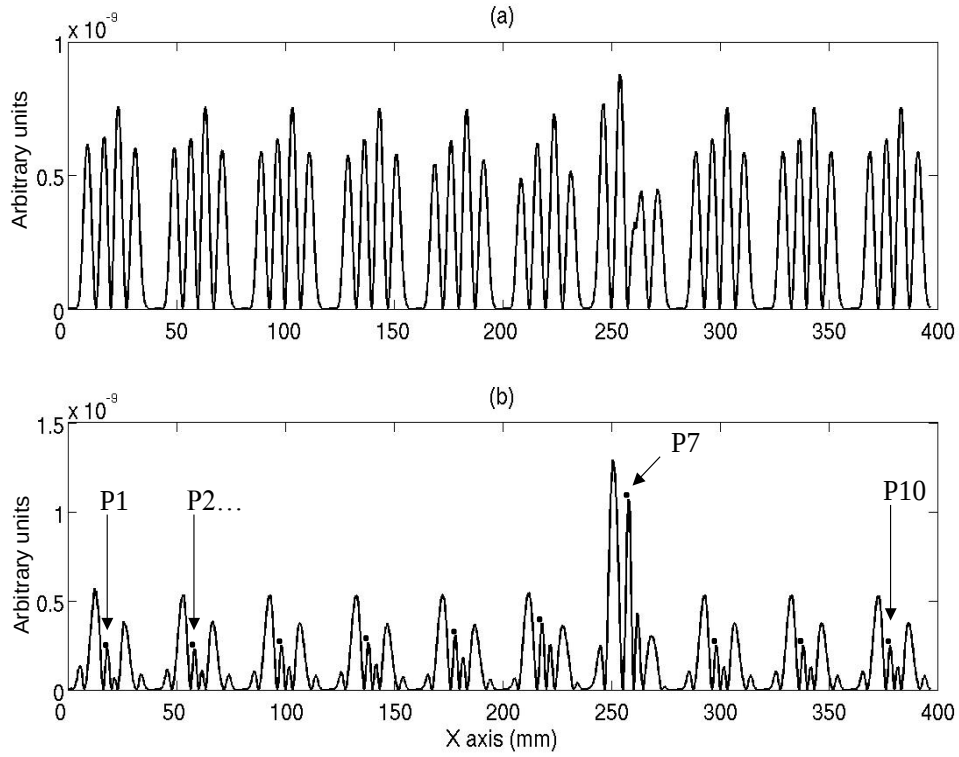

Figure 7. Results of the ICA applied to the EC data of Figure 4. a) Modulus of estimated source $\hat{\mathbf{s}}_1$, b) Modulus of estimated source $\hat{\mathbf{s}}_2$**;** S-mode data (continuous line), P-mode data (square markers).

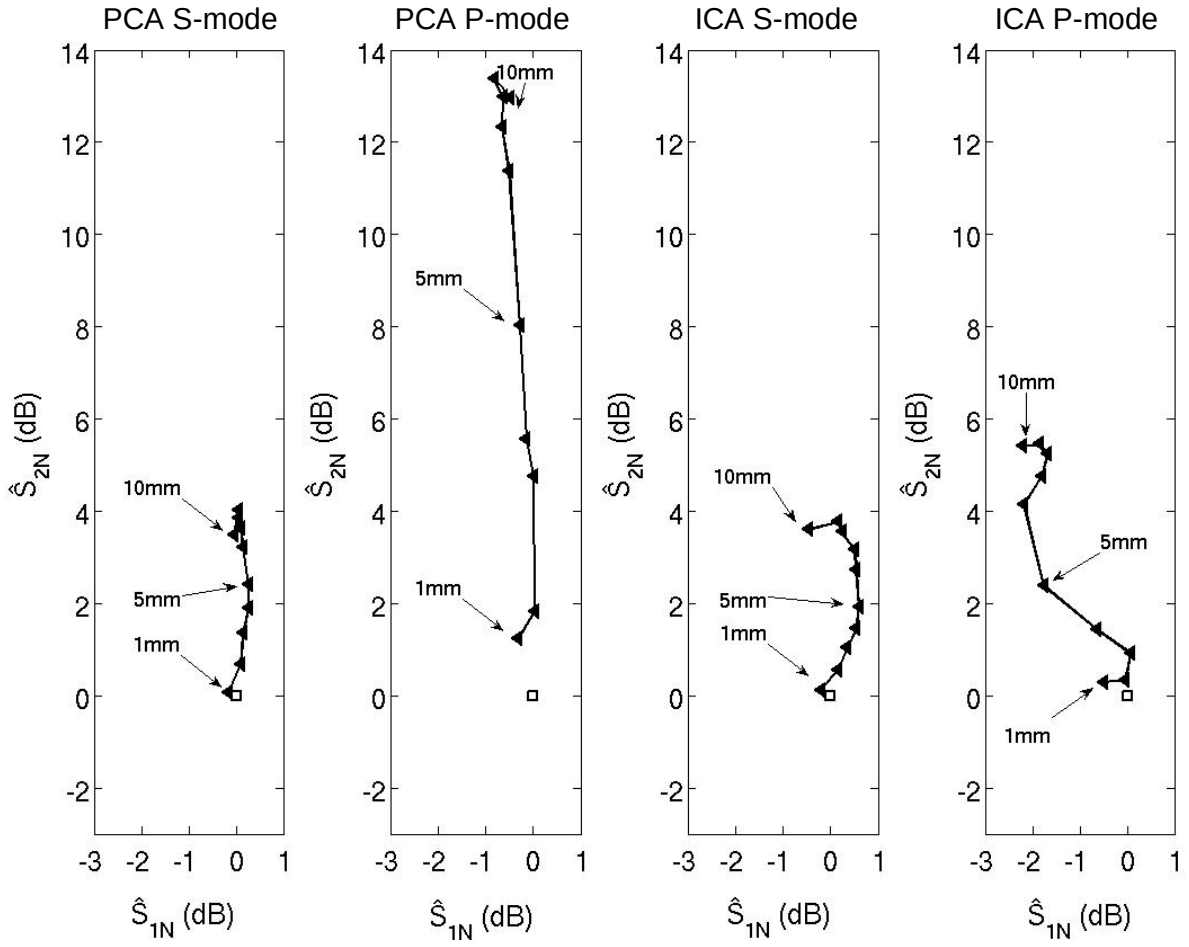

Figure 8. Separation efficiency of PCA and ICA methods, applied to the S-mode and P-mode EC data relative to the inspection of the reference sound rivet configuration (square markers) and flawed rivet configurations (triangle markers) for defect buried in plate n°2. Defect lengths range from 1 mm to 10 mm. The used EC frequency is f_2 = 1200 Hz.

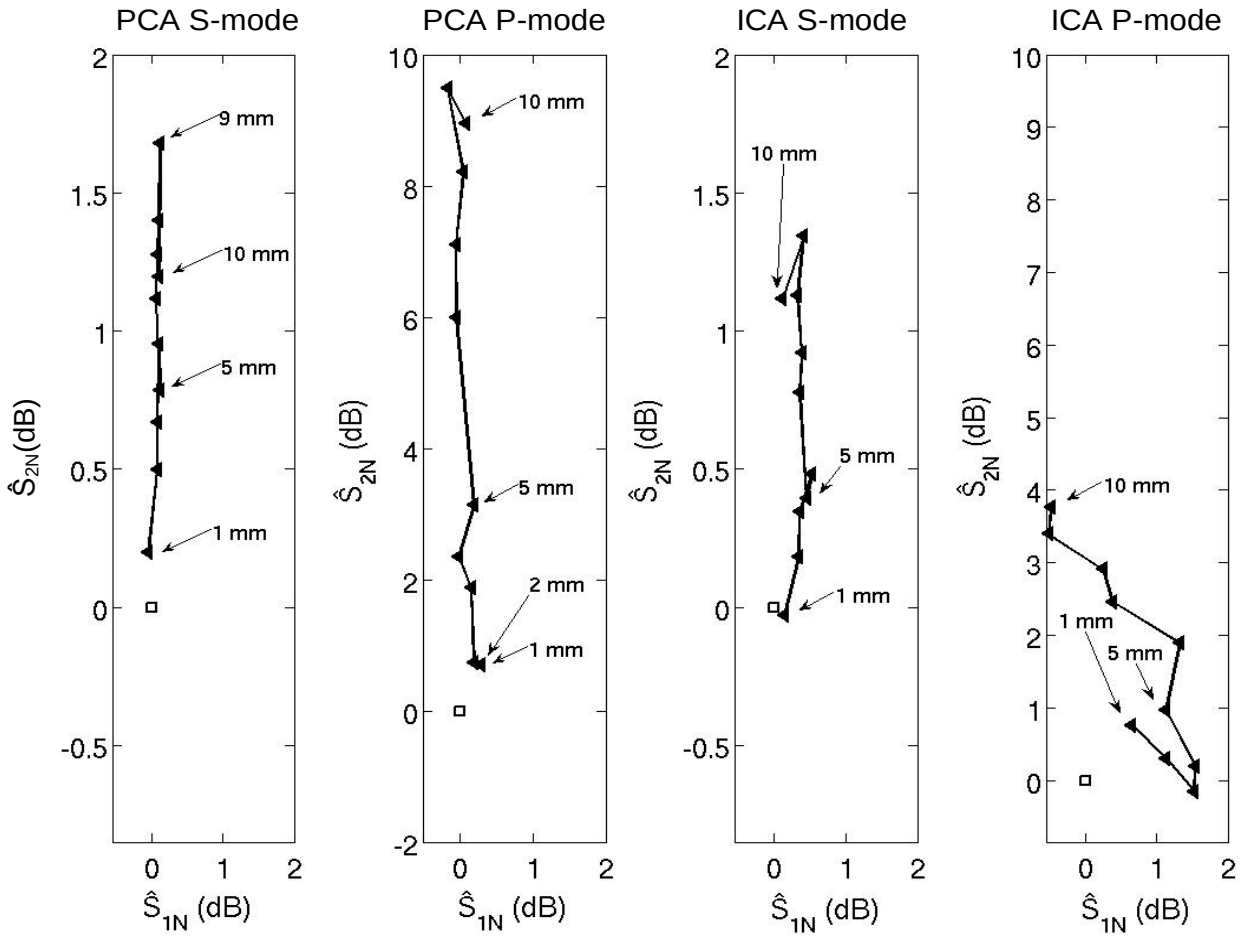

Figure 9. Separation efficiency of PCA and ICA methods, applied to the S-mode and P-mode EC data relative to the inspection of the reference sound rivet configuration (square markers) and flawed rivet configurations (triangle markers) for defects buried in plate n°3. Defect lengths range from 1 mm to 10 mm. The used EC frequency is f_3 = 600 Hz.

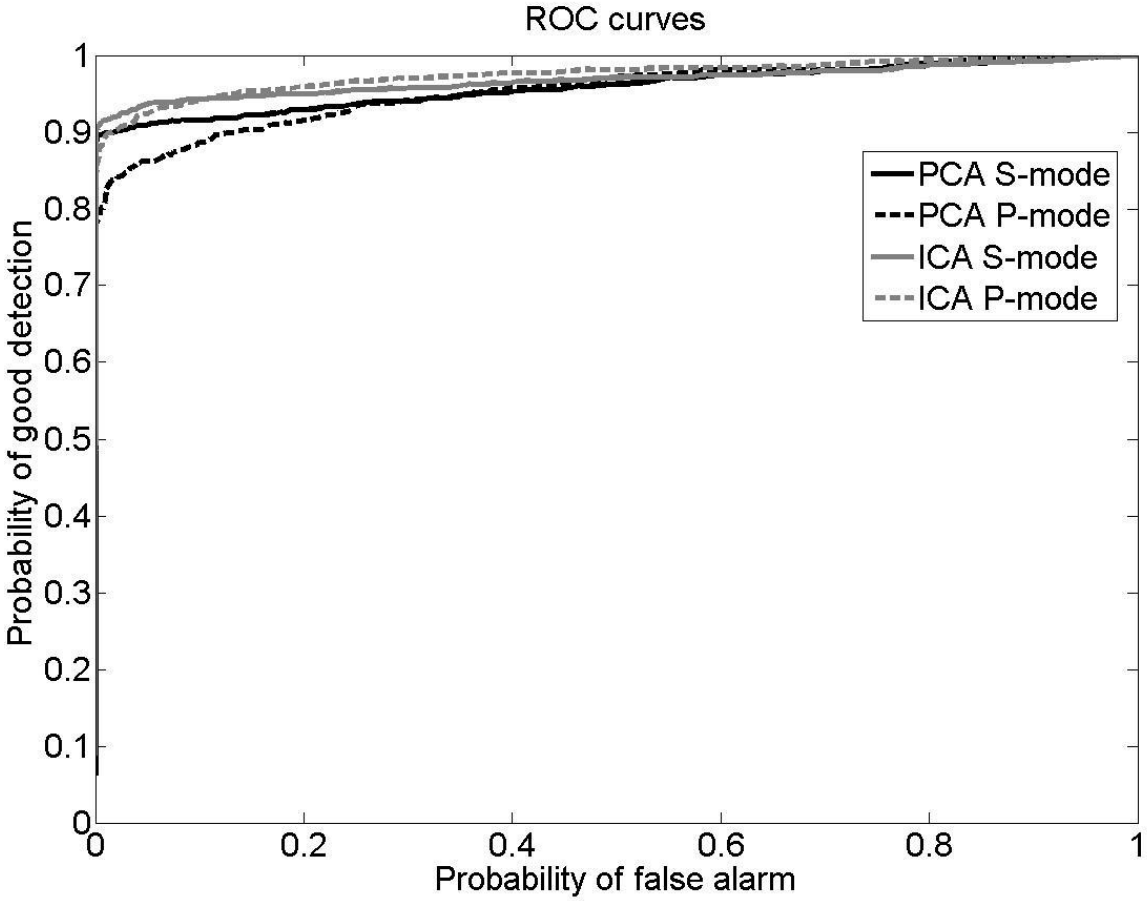

Figure 10. ROC curves relative to the detection of the defects buried in plate n°2, by the means of ICA and PCA applied onto S-mode and P-mode EC data. Defect lengths range from 1 mm to 10 mm (Table 1).

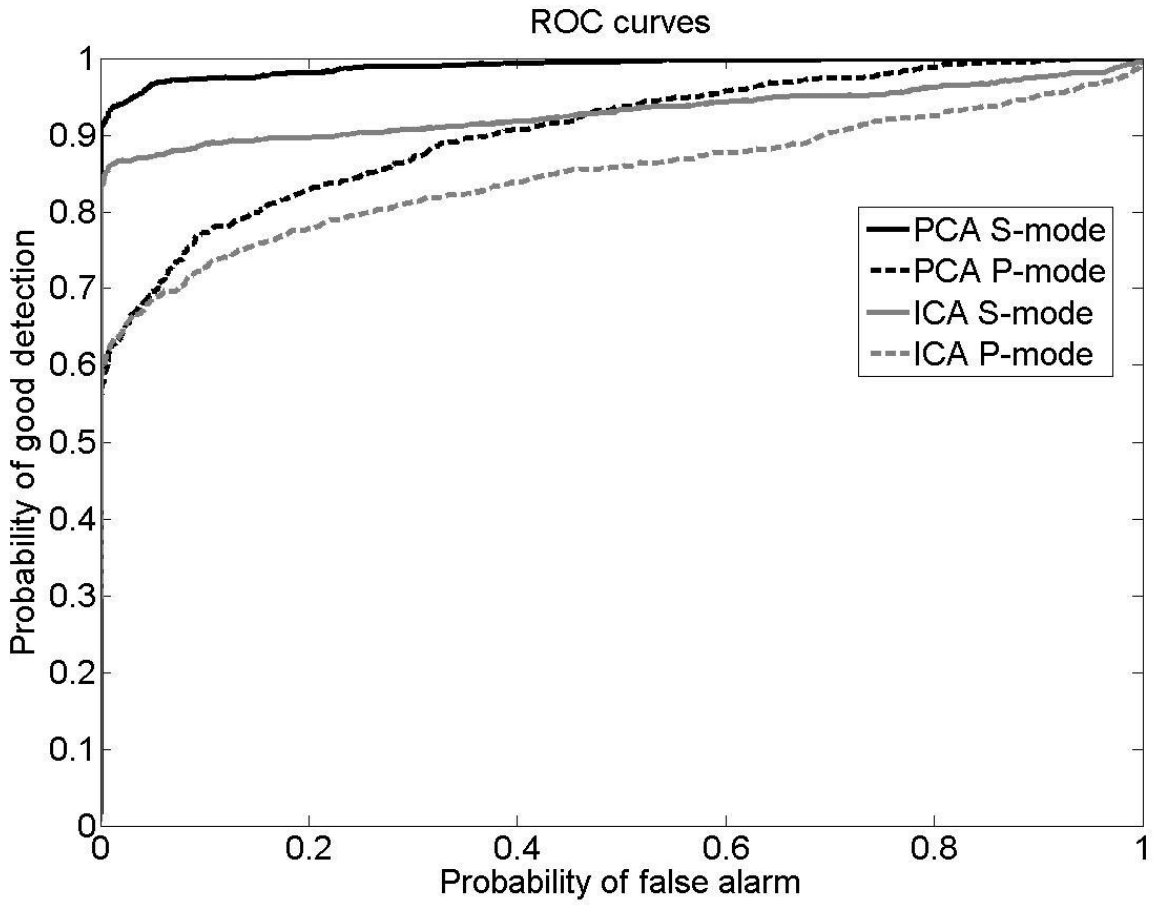

Figure 11. ROC curves relative to the detection of the defects buried in plate n°3, by the means of ICA and PCA applied onto S-mode and P-mode EC data. Defect lengths range from 1 mm to 10 mm (Table 1).

9. Tables

Depth in the lap joint	Notch height	Notch aperture	Notch length	Used EC frequency
Plate n°2	2 mm	500 µm	1, 2, 3… to 10 mm	f_2 = 1200 Hz
Plate n°3	2 mm	500 µm	1, 2, 3… to 10 mm	f_3 = 600 Hz

Table 1. Notch features and inspection frequency of the flawed rivet configurations

Depth in the lap joint	PCA S-mode	PCA P-mode	ICA S-mode	ICA P-mode
Plate n°2	0.958	0.956	0.963	0.976
Plate n°3	0.990	0.904	0.930	0.854

Table 2. Area under curve for the ROC curves relative to the defect detection

10. **Figure captions**

Figure 1. EC sensor configuration and inspected riveted lap joint

Figure 2. Operating modes

Figure 3. Array sensor general view and flat 8-layer circular pick-up coil array

Figure 4. EC signal obtained in S-mode (continuous line) and P-mode (square markers) at 1200Hz for the inspection of 10 rivets (9 rivets are sound, and the rivet in position P7 features a 5mm notch growing from the rivet, in plate 2. Amplitudes of in-phase and quadrature signals are in arbitrary units.

Figure 5. Lissajous plot of the EC signals of Figure 4, S-mode data (black lines: sound rivets; grey lines: flawed rivet) and P-mode data (square markers).

Figure 6. Results of the PCA applied to the EC data of Figure 4. a) Modulus of estimated source $\hat{\mathbf{s}}_1$, b) Modulus of estimated source $\hat{\mathbf{s}}_2$. S-mode data (continuous line), P-mode data (square markers).

Figure 7. Results of the ICA applied to the EC data of Figure 4. a) Modulus of estimated source $\hat{\mathbf{s}}_1$, b) Modulus of estimated source $\hat{\mathbf{s}}_2$; S-mode data (continuous line), P-mode data (square markers).

Figure 8. Separation efficiency of PCA and ICA methods, applied to the S-mode and P-mode EC data relative to the inspection of the reference sound rivet configuration (square markers) and flawed rivet configurations (triangle markers) for defect buried in plate n°2. Defect lengths range from 1 mm to 10 mm. The used EC frequency is f_2 = 1200 Hz.

Figure 9. Separation efficiency of PCA and ICA methods, applied to the S-mode and P-mode EC data relative to the inspection of the reference sound rivet configuration (square markers) and flawed rivet configurations (triangle markers) for defects buried in plate n°3. Defect lengths range from 1 mm to 10 mm. The used EC frequency is f_3 = 600 Hz.

Figure 10. ROC curves relative to the detection of the defects buried in plate n°2, by the means of ICA and PCA applied onto S-mode and P-mode EC data. Defect lengths range from 1 mm to 10 mm (Table 1).

Figure 11. ROC curves relative to the detection of the defects buried in plate n°3, by the means of ICA and PCA applied onto S-mode and P-mode EC data. Defect lengths range from 1 mm to 10 mm (Table 1).